Acta Oceanol. Sin., 2023, Vol. 42, No. 2, P. 29–43
https://doi.org/10.1007/s13131-022-2068-3
http://www.aosocean.com
E-mail: ocean2@hyxb.org.cn

Analysis of a simplification strategy in a nonhydrostatic model for surface and internal wave problems

Jinghua Zhang[1, 2], Wensheng Jiang[1, 3, 4*], Xueqing Zhang[1]

[1] Key Laboratory of Marine Environment and Ecology of Ministry of Education, Ocean University of China, Qingdao 266100, China

[2] Tianjin Research Institute for Water Transport Engineering, Ministry of Transport., Tianjin 300456, China

[3] Physical Oceanography Laboratory/Qingdao Collaborative Innovation Center of Marine Science and Technology, Ocean University of China, Qingdao 266100, China

[4] Pilot National Laboratory for Marine Science and Technology (Qingdao), Qingdao 266237, China

Received 12 December 2021; accepted 17 May 2022

© Chinese Society for Oceanography and Springer-Verlag GmbH Germany, part of Springer Nature 2023

Abstract

This paper examines the simplification strategy of retaining only the nonhydrostatic effect of local acceleration in a three-dimensional fully nonhydrostatic model regarding the submesoscale wave phenomenon in the ocean. Elaborate scale analysis of the vertical component of the Reynold-averaged Navier–Stokes (RANS) equation was performed, confirming the rationalization of this simplification. Then, the simplification was implemented in a RANS equation-based nonhydrostatic model NHWAVE (nonhydrostatic WAVE) to make a simplified nonhydrostatic model. Numerical examples were taken to test its performance, including surface sinusoidal waves propagating on an idealized East China Sea topography, tidally induced internal lee waves and small-scale solitary waves. The results show that in a considerably wide range of nonlinear strengths, the simplified nonhydrostatic model can obtain similar results as those in the fully nonhydrostatic model, even for smaller-scale solitary waves. Nonlinearity influences the applicability of the simplification. The stronger the nonlinearity is, the worse the simplified model describes the nonhydrostatic phenomenon. In general, the simplified nonhydrostatic model can simulate surface waves better than internal waves. Improvement of computational efficiency in the simplified nonhydrostatic model is reasonable, reducing the central processing unit time duration in the fully nonhydrostatic model by 16.4%–20.6%. The specially designed algorithm based on the simplified nonhydrostatic equation can remarkably reduce the computational time.

Key words: simplification of nonhydrostatic model, submesoscale wave, internal lee wave

Citation: Zhang Jinghua, Jiang Wensheng, Zhang Xueqing. 2023. Analysis of a simplification strategy in a nonhydrostatic model for surface and internal wave problems. Acta Oceanologica Sinica, 42(2): 29–43, doi: 10.1007/s13131-022-2068-3

1 Introduction

Reynolds-averaged Navier–Stokes (RANS) equations can describe hydrodynamic processes ranging from small-scale waves to large-scale ocean circulation in theory. However, when a specific phenomenon is studied with limited computational resources, the approximation form of the RANS equations is often employed in ocean modeling. For example, the hydrostatic approximation, ignoring the acceleration in the vertical direction for large-scale and mesoscale processes, is widely used in ocean circulation models. However, it does not work at all temporal and spatial scales, especially when the local derivative becomes essential for small-scale processes. When the horizontal scale of the motion is comparable with its vertical scale, the nonhydrostatic effect becomes apparent and needs to be involved (Marshall et al., 1997a; Casulli, 1999). It has been proven that the hydrostatic approximation is not valid for flows over rapidly varying slopes (Casulli and Zanolli, 2002). The nonhydrostatic effect leads to frequency dispersion: waves of different frequencies will gradually depart as they propagate. This effect opposes the nonlinear wave steepening. When the nonhydrostatic dispersion effect and nonlinear steepening come into balance, a solitary wave will form.

For natural phenomena such as extreme tsunamis (Ma et al., 2012; Choi et al., 2014; Ai et al., 2021a) or large-amplitude internal waves in the ocean (Berntsen et al., 2008; Lai et al., 2010a, 2010b; Zhang et al., 2011), there are both hydrostatic and nonhydrostatic numerical studies. However, an increasing number of studies have proven the significance of the nonhydrostatic effect by comparing it with observations. To capture the nonhydrostatic effect accurately, more terms should be included in the vertical momentum equation, rather than retaining only the vertical pressure gradient and the gravity force for the hydrostatic approximation. In one-dimensional and two-dimensional simulations, some theoretical nonhydrostatic models, such as the KdV and Boussinesq models, are widely used to simulate nonhydrostatic surface waves and internal waves. Fully nonhydrostatic models, which retain all terms in the RANS equations, are widely applied in three-dimensional simulations. Nearly all the nonhydrostatic models are developed based on this frame, such as MITgcm (Marshall et al., 1997b), FVCOM-NH (Lai et al., 2010a, b), BOM (Berntsen, 2004), SWASH (Stelling and Zijlema, 2003; Zijlema et al., 2011), SUNTANS (Fringer et al., 2006), nonhydrostatic WAVE (Ma et al., 2012; Shi et al., 2015), ROMS-NH (Kanarska

Foundation item: The National Natural Science Foundation of China under contract No. 41676003.
*Corresponding author, E-mail: wsjang@ouc.edu.cn

et al., 2007), and POM-NH (Kanarska and Maderich, 2003) and nonhydrostatic models for surface waves (Ai et al., 2019, 2021a; He et al., 2020) and internal waves (Ai et al., 2021b), etc. Most of these nonhydrostatic models utilize the pressure decomposition method, and a nonhydrostatic pressure is introduced by adding a nonhydrostatic pressure gradient in the vertical direction. The resulting horizontal velocity is forced via the nonhydrostatic pressure gradients by the local divergence or convergence in the model cells. However, nonhydrostatic models use much more central processing unit (CPU) time than their hydrostatic counterparts by one or several orders of magnitude due to the effort in solving a Poisson equation of the nonhydrostatic pressure (Shi et al., 2015; Liu et al., 2016). Massive data storage in nonhydrostatic models is also a great challenge. These issues significantly limit the broader application of nonhydrostatic models.

To overcome this limitation, researchers have proposed different ways to expand the applicability of nonhydrostatic models. On the one hand, some numerical techniques are adopted, such as the grid-switching strategy (Botelho et al., 2009), the improvement of the efficiency of the Poisson solver (Matsumura and Hasumi, 2008), and the selection of an appropriate coarser resolution (Berntsen et al., 2009). On the other hand, the hydrodynamic equations are simplified according to the properties of certain processes. To be more specific, we can only retain the dominant terms in the RANS equation and eliminate some unimportant terms, making the numerical simulation easier to understand physically and resource savings for the calculation.

In this paper, we focus on the submesoscale waves with a typical horizontal scale of hundreds of meters to kilometers and study the applicability of a simplified nonhydrostatic model. Submesoscale movement, which is between small-scale (10^{-1}–10^{2} m) and mesoscale (10^{4}–10^{5} m), is in the interval in which the nonhydrostatic effect becomes essential (Mahadevan, 2006; Thomas et al., 2008). It can refer to a wide range of processes in the ocean, including submesoscale coherent vortices, submesoscale surface waves, and internal gravity waves in submesoscale regimes. These submesoscale processes play crucial roles in bridging mesoscale to small-scale processes, especially in the upper ocean. As large-scale waves propagate from the open sea to coastal areas, their horizontal length scale becomes shorter and shorter, and these waves may belong to submesoscales.

A simplification strategy that only adds the vertical local derivative term in the hydrostatic balance in barotropic flow is studied by several researchers with regard to the submesoscale process. For depth-averaged models, Yamazaki et al. (2009, 2011), Lu et al. (2015) applied this simplification for simulating tsunami propagation and nearshore wave propagation. Zijlema and Stelling (2008) and Zijlema et al. (2011) studied surface waves and rapidly varying flows. Aricò and Re (2016) simulated various kinds of flooding processes.

However, in a stratified fluid, this simplification method has not been well examined. Daily and Imberger (2003) applied it in a Boussinesq model and simulated internal solitary waves propagating near the surface. They proved that the simplified nonhydrostatic model could drastically improve wave propagation in the hydrostatic model, but problems such as the spreading of pycnoclines remain. Currently, work on the application of this simplification in a three-dimensional nonhydrostatic model is still very limited. It remains to be known if it will work well in a such kind nonhydrostatic model. Resolving this problem will help to improve the computational efficiency of nonhydrostatic models and extend their applicability.

In this paper, the simplification strategy of only retaining the local vertical acceleration will be implemented in the framework of a three-dimensional nonhydrostatic wave model NHWAVE (Ma et al., 2012; Shi et al., 2015). Comparisons are made among the fully nonhydrostatic model, the simplified nonhydrostatic model, and the hydrostatic model to validate the performance of the simplification strategy. The paper is organized as follows. Section 2 validates the simplification based on a scale analysis and introduces the corresponding simplified governing momentum equations. We also present the standard of measuring the nonhydrostatic effect and provide a criterion to evaluate the performance of a simplified nonhydrostatic model. In Section 3, two numerical applications are described to validate the simplification strategy of the nonhydrostatic model, including surface sinusoidal waves over a continental shelf and internal lee waves induced by flow over a sill. In Section 4, an extended application of the simplified nonhydrostatic model to smaller-scale solitary waves is discussed. Discussions about the applicability of the simplification concerning the nonlinearity and the computational efficiency improvement are also made. Brief conclusions are given in Section 5.

2 Methods

2.1 *Scale analysis of vertical momentum equation*

Scale analysis of the vertical component of RANS equation is clarified on the submesoscale surface wave and internal wave in this section. For simplicity, the tide-generating force and the Coriolis force are neglected in this study. Thus, the vertical momentum equation in Cartesian coordinates is given as

$$\underbrace{\frac{\partial w}{\partial t}}_{\substack{\text{local}\\ \text{derivative}}} + \underbrace{u\frac{\partial w}{\partial x} + v\frac{\partial w}{\partial y}}_{\text{advection}} + \underbrace{w\frac{\partial w}{\partial z}}_{\text{convection}} = \underbrace{-\frac{1}{\rho}\frac{\partial p}{\partial z}}_{\text{pressure gradient}} - \underbrace{g}_{\text{gravity}} + \underbrace{A_{\mathrm{H}}\left(\frac{\partial^2 w}{\partial x^2} + \frac{\partial^2 w}{\partial y^2}\right)}_{\substack{\text{horizontal}\\ \text{turbulent viscosity}}} + \underbrace{A_{\mathrm{V}}\frac{\partial^2 w}{\partial z^2}}_{\substack{\text{vertical}\\ \text{turbulent viscosity}}}, \tag{1}$$

where t is time, x, y, z are eastward, northward, and upward indices of coordinates, respectively, and $u(x, y, z, t)$, $v(x, y, z, t)$, and $w(x, y, z, t)$ are the corresponding velocity components in the x, y, z direction. ρ is the density, p is the pressure, g is the gravitational acceleration, A_{H} and A_{V} are the eddy viscosities in the horizontal and vertical directions, respectively. Variables can be written in the nondimensional form with

$$\begin{aligned} &(\bar{x}, \bar{y}) = (x, y)/L, \quad \bar{z} = z/D, \quad \bar{t} = t/T, \\ &(\bar{u}, \bar{v}) = (u, v)/U, \quad \bar{w} = w/W, \quad \bar{p} = p/P, \end{aligned} \tag{2}$$

where L and D are the characteristic horizontal and vertical scales, respectively, T is the time scale, W is the vertical velocity scale, and P is the pressure scale. Substituting Eq. (2) into Eq. (1) yields the nondimensional form of the vertical momentum equation

$$\frac{W}{T}\frac{\partial \bar{w}}{\partial \bar{t}} + \frac{UW}{L}\left(\bar{u}\frac{\partial \bar{w}}{\partial \bar{x}} + \bar{v}\frac{\partial \bar{w}}{\partial \bar{y}}\right) + \frac{W^2}{D}\bar{w}\frac{\partial \bar{w}}{\partial \bar{z}} = -\frac{P}{\rho D}\frac{\partial \bar{p}}{\partial \bar{z}} - g + \frac{A_{\mathrm{H}}W}{L^2}\left(\frac{\partial^2 \bar{w}}{\partial \bar{x}^2} + \frac{\partial^2 \bar{w}}{\partial \bar{y}^2}\right) + \frac{A_{\mathrm{V}}W}{D^2}\frac{\partial^2 \bar{w}}{\partial \bar{z}^2}. \tag{3}$$

Characteristic scales of physical variables defined in Eq. (2) vary with phenomena and influence the relative importance of

terms in Eq. (3). This paper intends to find the predominant term controlling submesoscale waves, including surface waves and internal gravity waves. Here, we introduce the scale analysis processes for surface waves and internal waves separately.

2.1.1 *Scale analysis for surface gravity wave*

For a long surface gravity wave, the leading order balance is between the local inertial force and the pressure gradient force formed by the sea surface slope, i.e.,

$$\frac{\partial u}{\partial t} \sim g\frac{\partial \zeta}{\partial x}, \tag{4}$$

where ζ denotes the dimensional surface water elevation. The scale balance of Eq. (4) is

$$\frac{U}{T} \sim g\frac{A}{L}, \tag{5}$$

where A represents the characteristic orders of magnitude of surface water elevation, which is generally given by A=10^{-1} m. The characteristic scale of time T should be coincident with the horizontal scale L and the phase speed of the long gravity wave $C=\sqrt{gD}$, thus

$$T \sim \frac{L}{C}. \tag{6}$$

Combining Eq. (5) and Eq. (6), we define a dimensionless parameter κ

$$\kappa = \frac{U}{C} = \frac{A}{D}. \tag{7}$$

Both horizontal velocity and vertical velocity components exist in the local divergence-free continuity equation, $\frac{\partial u}{\partial x}+\frac{\partial v}{\partial y}+\frac{\partial w}{\partial z}=0$, so

$$\frac{U}{L} \sim \frac{W}{D}. \tag{8}$$

Divide both sides of Eq. (3) by $\frac{W}{T}$, the characteristic scales of the local derivative in the vertical direction, and after some algebra with considering Eq. (7) and Eq. (8), we obtain

$$\frac{\partial \overline{w}}{\partial \overline{t}}+\kappa\left(\bar{u}\frac{\partial \overline{w}}{\partial \bar{x}}+\bar{v}\frac{\partial \overline{w}}{\partial \bar{y}}+\overline{w}\frac{\partial \overline{w}}{\partial \bar{z}}\right) = -\frac{P}{\rho D}\frac{T}{W}\frac{\partial p}{\partial z}-\frac{T}{W}g+ \frac{A_{\mathrm{H}}T}{L^2}\left(\frac{\partial^2 \overline{w}}{\partial \bar{x}^2}+\frac{\partial^2 \overline{w}}{\partial \bar{y}^2}\right)+\frac{A_{\mathrm{V}}T}{D^2}\frac{\partial^2 \overline{w}}{\partial \bar{z}^2}. \tag{9}$$

From Eq. (9), it can be seen that κ defined in Eq. (7) can measure the strength of nonlinear terms. This shows that we can use two methods, either $\frac{U}{C}$ the ratio of the horizontal velocity of water particles to the phase speed of the wave or $\frac{A}{D}$, the ratio of surface water elevation to the static depth as a criterion to discuss the nonlinearity of the long surface gravity wave.

For a submesoscale surface wave, to make scale analysis, we take the lower limit of horizontal scale of mesoscale process (i.e., 10 km) as the characteristic wavelength and assume a characteristic water depth in the marginal sea, D=10^3 m. The horizontal velocity is given by 10^{-2} m/s. The characteristic period T and vertical velocity W can be deduced based on Eq. (6) and Eq. (8). Characteristic scales of all the variables are listed in Table 1. By substituting them into Eq. (9), the typical magnitudes of every single force in Eq. (9) can be obtained (Table 2).

As shown in Table 2, the primary balance of the submesoscale surface wave is between the pressure gradient force and the gravity force. It is the so-called hydrostatic approximation, for which the vertical acceleration of the water mass is ignored, and the vertical momentum Eq. (1) reduces to a diagnostic equation as

$$0 = -\frac{1}{\rho}\frac{\partial p}{\partial z}-g. \tag{10}$$

The hydrostatic approximation is accurate for large-scale processes and is widely used when modeling large and mesoscale processes such as circulation and barotropic tidal waves. However, the hydrostatic model cannot reflect nonhydrostatic features of waves (Yamazaki et al., 2009, 2011; Wei and Jia, 2014), especially for smaller-scale waves. A higher-order approximation of Eq. (1) should be made to reflect the nonhydrostatic effect. In Table 2, the local derivative is the largest among the remaining terms, followed by the nonlinearity term apart from the two forces in the hydrostatic approximation. The former is three orders of magnitude larger than the latter. This indicates that we may only add the local derivative term to include the major part of the nonhydrostatic effect in a model. Then, the vertical momentum equation can be given by

$$\frac{\partial w}{\partial t} = -\frac{1}{\rho_0}\left(\frac{\partial p}{\partial z}+g\rho\right). \tag{11}$$

From the above scale analysis, we verify that adding the local

Table 1. Characteristic scale of variables for submesoscale surface wave

Variable	D/m	L/m	U/(m·s^{-1})	W/(m·s^{-1})	T/s	A_{H}/(m^2·s^{-1})	A_{V}/(m^2·s^{-1})
Magnitude	1×10^3	1×10^4	1×10^{-2}	1×10^{-3}	1×10^2	1×10^{-3}–1×10^{-1}	1×10^{-4}–1×10^{-2}

Table 2. The magnitude of every term in the vertical momentum equation

Force	Local derivative	Advection	Convection	Pressure gradient	Gravity	Horizontal eddy viscosity	Vertical eddy viscosity
Formula	1	$\kappa=\frac{A}{D}$	$\kappa=\frac{A}{D}$	$-\frac{P}{\rho^{\mathrm{a}}D}\frac{T}{W}$	$\frac{T}{W}g^{\mathrm{b}}$	$\frac{A_{\mathrm{H}}T}{L^2}$	$\frac{A_{\mathrm{V}}T}{D^2}$
Magnitude	1	1×10^{-3}	1×10^{-3}	–1×10^6	1×10^6	1×10^{-7}	1×10^{-6}

Note: [a] ρ=10^3 kg/m^3; [b] $g\approx$10 m/s^2.

derivative term in the hydrostatic approximation simplifies the fully nonhydrostatic model when the surface gravity wave is considered. This simplification strategy of the fully nonhydrostatic momentum equation is the starting point of this research. This simplification at least has significance in two aspects. On the one hand, discussing the physical mechanism may be more concise when only focusing on the primary term that controls a specific process. On the other hand, eliminating some unimportant forces in the governing equation will undoubtedly save computational resources and increase the calculation efficiency.

2.1.2 *Scale analysis for internal lee wave*

In the stratified ocean, density varies by at most a few percentage points. We replace density ρ in Eq. (1) by a constant value ρ_0 (with the exception of the gravity term), so the vertical momentum equation becomes

$$\frac{\partial w}{\partial t}+u\frac{\partial w}{\partial x}+v\frac{\partial w}{\partial y}+w\frac{\partial w}{\partial z}=-\frac{1}{\rho_0}\frac{\partial p}{\partial z}-\frac{\rho}{\rho_0}g+A_{\mathrm{H}}\left(\frac{\partial^2 w}{\partial x^2}+\frac{\partial^2 w}{\partial y^2}\right)+A_{\mathrm{V}}\frac{\partial^2 w}{\partial z^2}. \tag{12}$$

An internal wave can be seen as a perturbation of a static background state that has only vertical dependence so that we can divide variables into two parts: one part is related to the static background field, and the other part is associated with the internal wave motion (the variable with a prime)

$$\begin{aligned} p&=p_0(z)+p'(t,\vec{x}),\\ \rho&=\rho_0(z)+\rho'(t,\vec{x}), \end{aligned} \tag{13}$$

the static field obeys the hydrostatic balance

$$\frac{\mathrm{d}p_0}{\mathrm{d}z}=-\rho_0 g, \tag{14}$$

so Eq. (12) can be written as

$$\underbrace{\frac{\partial w}{\partial t}}_{\text{local derivative}}+\underbrace{u\frac{\partial w}{\partial x}+v\frac{\partial w}{\partial y}}_{\text{advection}}+\underbrace{w\frac{\partial w}{\partial z}}_{\text{convection}}=\underbrace{-\frac{1}{\rho_0}\frac{\partial p'}{\partial z}}_{\text{pressure gradient}}-\underbrace{\frac{\rho'}{\rho_0}g}_{\text{gravity}}+\underbrace{A_{\mathrm{H}}\left(\frac{\partial^2 w}{\partial x^2}+\frac{\partial^2 w}{\partial y^2}\right)}_{\substack{\text{horizontal}\\ \text{turbulent viscosity}}}+\underbrace{A_{\mathrm{V}}\frac{\partial^2 w}{\partial z^2}}_{\substack{\text{vertical}\\ \text{turbulent viscosity}}}. \tag{15}$$

For internal wave phenomenon, we introduced the vertical velocity scale W and the vertical scale over which the internal wave field varies by one order of magnitude H, and the dimensionless form of Eq. (15) is presented by

$$\frac{W}{T}\frac{\partial \overline{w}}{\partial \overline{t}}+\frac{UW}{L}\left(\bar{u}\frac{\partial \overline{w}}{\partial \bar{x}}+\bar{v}\frac{\partial \overline{w}}{\partial \bar{y}}\right)+\frac{W^2}{H}\overline{w}\frac{\partial \overline{w}}{\partial \bar{z}}=-\frac{P}{\rho_0 H}\frac{\partial p'}{\partial \bar{z}}-\frac{\rho'}{\rho_0}g+\frac{A_{\mathrm{H}}W}{L^2}\left(\frac{\partial^2 \overline{w}}{\partial \bar{x}^2}+\frac{\partial^2 \overline{w}}{\partial \bar{y}^2}\right)+\frac{A_{\mathrm{V}}W}{H^2}\frac{\partial^2 \overline{w}}{\partial \bar{z}^2}. \tag{16}$$

The leading order balance for long gravity internal waves is also between the local inertial force and the pressure gradient force, i.e.,

$$\rho_0\frac{U}{T}\sim\frac{P}{L}. \tag{17}$$

Similar to surface waves, the characteristic time scale should be expressed by the horizontal scale and the phase speed of the long gravity wave as

$$T\sim\frac{L}{C}, \tag{18}$$

therefore,

$$P\sim\rho_0 CU. \tag{19}$$

The typical phase speed of the internal wave C is on the order of 1 m/s in the ocean. Dividing Eq. (16) by the characteristic scales of the local derivative, $\frac{W}{T}$, yields

$$\frac{\partial \overline{w}}{\partial \bar{t}}+\frac{U}{C}\left(\bar{u}\frac{\partial \overline{w}}{\partial \bar{x}}+\bar{v}\frac{\partial \overline{w}}{\partial \bar{y}}+\overline{w}\frac{\partial \overline{w}}{\partial \bar{z}}\right)=-\frac{CU}{H}\frac{T}{W}\frac{\partial p'}{\partial \bar{z}}-\frac{\rho'}{\rho_0}\frac{T}{W}g+\frac{A_{\mathrm{H}}T}{L^2}\left(\frac{\partial^2 \overline{w}}{\partial \bar{x}^2}+\frac{\partial^2 \overline{w}}{\partial \bar{y}^2}\right)+\frac{A_{\mathrm{V}}T}{H^2}\frac{\partial^2 \overline{w}}{\partial \bar{z}^2}, \tag{20}$$

in which we define $Fr=\frac{U}{C}$ to measure the importance of nonlinearity.

Taking the submesoscale internal lee-wave as an example, the horizontal scale for internal waves is shorter than the surface wave. What is more, the characteristic vertical scale is no longer the whole depth and can be approximated by the amplitude of internal waves with dozen meters. Substitute the characteristic scales of variables (summarized in Table 3) into Eq. (20), we obtain the typical magnitudes of each force (Table 4) for the internal lee wave.

From Table 4, we can obtain a similar conclusion with those in scale analysis for surface waves, i.e., the local derivative term is the most prominent term except for two prevailing terms in the hydrostatic approximation, followed by nonlinearity. Therefore, we can only retain the prominent local derivative term to include the major nonhydrostatic effect, and the simplified vertical equation can be presented as

Table 3. The characteristic scale of variables for submesoscale internal wave

Variables	H/m	L/m	U/(m·s^{-1})	W/(m·s^{-1})	T/s	A_{H}/(m^2·s^{-1})	A_{V}/(m^2·s^{-1})
Magnitude	1×10^{-3}	1×10^{-3}	-1×10^{6}	1×10^{6}	1×10^{-7}	1×10^{-6}	1×10^{-3}

Table 4. The magnitude of every term in the vertical momentum equation

Force	Local derivative	Advection	Convection	Pressure gradient	Gravity	Horizontal eddy viscosity	Vertical eddy viscosity
Formula	1	$Fr=\frac{U}{C}$	$Fr=\frac{U}{C}$	$-\frac{CU}{H}\frac{T}{W}$	$\frac{\rho'^{\mathrm{b}}}{\rho_0{}^{\mathrm{a}}}\frac{T}{W}g^{\mathrm{c}}$	$\frac{A_{\mathrm{H}}T}{L^2}$	$\frac{A_{\mathrm{V}}T}{D^2}$
Magnitude	1	1×10^{-2}	1×10^{-2}	-1×10^{3}	1×10^{3}	1×10^{-4}–1×10^{-2}	1×10^{-5}–1×10^{-3}

Note: [a]$\rho_0=10^3$ kg/m^3; [b]$\rho'=10$ kg/m^3; [c]g $\approx$10 m/s^2.

$$\frac{\partial w}{\partial t} = -\frac{1}{\rho_0}\frac{\partial p}{\partial z} + \frac{\rho'}{\rho_0}g. \tag{21}$$

By comparing Table 2 and Table 4, we can find that the prominent local derivative is only two orders larger in magnitude than the nonlinearity term in Table 4, while in scale analysis for surface wave (Table 2), the difference between local derivative and nonlinearity can be up to three or four orders in magnitude. It indicates that there may be a lower level of prominence for local derivative term in simulating internal waves.

To conclude, we may construct a simplified nonhydrostatic model in a three-dimensional simulation for submesoscale surface waves and internal gravity waves. This paper will implement this simplification strategy based on a three-dimensional fully nonhydrostatic model NHWAVE and make a simplified nonhydrostatic model.

2.2 *The simplification of the NHWAVE model*

The simplification of a fully nonhydrostatic model major involves the simplification of the calculation process. The model used in this study is based on the modeling framework of the Nonhydrostatic Wave model, NHWAVE (Ma et al., 2012; Shi et al., 2015). It is a three-dimensional fully nonhydrostatic wave model formulated by solving the RANS equations in the σ coordinate system. Hybrid finite volume-finite difference schemes are used. NHWAVE has been widely used and is proved to be capable of simulating both surface waves (Ma et al., 2012; Derakhti et al., 2015) and internal waves as well as mixing in stratified fluid (Ma et al., 2013; Shi et al., 2017, 2019; Zhou et al.,2017). Although the NHWAVE model is implemented in a terrain and surface-following σ coordinate system, we describe the equation in Cartesian coordinates for clarity.

The pressure decomposition method is utilized in NHWAVE by separating the whole pressure $p(x,y,z,t)$ into its hydrostatic and nonhydrostatic components $p_{\mathrm{HY}}(x,y,z,t)$ and $q(x,y,z,t)$. The momentum equations can be written as

$$\frac{\partial u}{\partial t}+u\frac{\partial u}{\partial x}+v\frac{\partial u}{\partial y}+w\frac{\partial u}{\partial z} = -\frac{1}{\rho_0}\frac{\partial p_{\mathrm{HY}}}{\partial x}-\frac{1}{\rho_0}\frac{\partial q}{\partial x}+ A_{\mathrm{H}}\left(\frac{\partial^2 u}{\partial x^2}+\frac{\partial^2 u}{\partial y^2}\right)+\frac{\partial}{\partial z}\left(A_{\mathrm{V}}\frac{\partial u}{\partial z}\right), \tag{22}$$

$$\frac{\partial v}{\partial t}+u\frac{\partial v}{\partial x}+v\frac{\partial v}{\partial y}+w\frac{\partial v}{\partial z} = -\frac{1}{\rho_0}\frac{\partial p_{\mathrm{HY}}}{\partial y}-\frac{1}{\rho_0}\frac{\partial q}{\partial y}+ A_{\mathrm{H}}\left(\frac{\partial^2 v}{\partial x^2}+\frac{\partial^2 v}{\partial y^2}\right)+\frac{\partial}{\partial z}\left(A_{\mathrm{V}}\frac{\partial v}{\partial z}\right), \tag{23}$$

$$\frac{\partial w}{\partial t}+u\frac{\partial w}{\partial x}+v\frac{\partial w}{\partial y}+w\frac{\partial w}{\partial z} = -\frac{1}{\rho_0}\frac{\partial p_{\mathrm{HY}}}{\partial z}-\frac{1}{\rho_0}\frac{\partial q}{\partial z}-\frac{\rho}{\rho_0}g+ A_{\mathrm{H}}\left(\frac{\partial^2 w}{\partial x^2}+\frac{\partial^2 w}{\partial y^2}\right)+A_{\mathrm{V}}\frac{\partial^2 w}{\partial z^2}. \tag{24}$$

The continuity equation is written as

$$\frac{\partial u}{\partial x}+\frac{\partial v}{\partial y}+\frac{\partial w}{\partial z} = 0. \tag{25}$$

In this paper, the importance of the local derivative term in the vertical direction is noticed in the nonhydrostatic model, so the vertical component of governing Eq. (24) can be simplified as follows.

$$\frac{\partial w}{\partial t} = \underline{-\frac{1}{\rho_0}\frac{\partial p_{\mathrm{HY}}}{\partial z}-g\frac{\rho}{\rho_0}}_{=0}-\frac{1}{\rho_0}\frac{\partial q}{\partial z}, \tag{26}$$

in which the hydrostatic pressure gradient is balanced by the buoyancy term (underlined in Eq. (26)), so the vertical momentum equation is simplified into the approximation form

$$\frac{\partial w}{\partial t} = -\frac{1}{\rho_0}\frac{\partial q}{\partial z}. \tag{27}$$

The numerical scheme and the calculation procedure can be kept the same as the original NHWAVE model, which adopts the combined finite-volume and finite-difference algorithm with a Godunov-type (shock-capturing algorithm) for spatial discretization. For temporal discretization, the two-stage strong stability-preserving Runge–Kutta algorithm is used, in which a typical two-step projection method is used twice. To implement the projection method, one separates the solution into hydrostatic and nonhydrostatic parts and solves them sequentially. In the first step, the contribution from the nonhydrostatic pressure is neglected, and in the second step, the velocities are corrected by including nonhydrostatic pressure terms. We take the n to $n+1$ time steps as an example to illustrate the simplification of the calculation in NHWAVE.

In the first stage of the Runge–Kutta algorithm, an intermediate velocity $U^{(1)} = (u^{(1)}, v^{(1)}, w^{(1)})^{\mathrm{T}}$ is obtained by the two-step projection method indicated by Eqs (28) and (29).

Step 1: Hydrostatic part

$$\frac{\boldsymbol{U}^* - \boldsymbol{U}^n}{\Delta t} = \boldsymbol{F}^n, \tag{28}$$

where $\boldsymbol{U}^* = (u^*, v^*, w^*)^{\mathrm{T}}$ is the provisional velocity after the first step of the calculation. In a fully nonhydrostatic model, $\boldsymbol{F}^n = (F_x^n, F_y^n, F_z^n)^{\mathrm{T}}$ indicates the sum of convection, the hydrostatic pressure gradient term, the gravity, and the viscosity terms in the original momentum equation (i.e., all terms in Eqs (22)–(24) while neglecting the local derivative and the nonhydrostatic pressure gradient). By employing the simplification method in this paper, the vertical momentum Eq. (24) is simplified into Eq. (27), $\boldsymbol{F}_z^n$ becomes zero, and the vertical velocity w^* will be as exact as w^n without calculation. Thus, in the simplified nonhydrostatic model, the computation cost will be reduced in this step.

Step 2: Nonhydrostatic part

$$\frac{\boldsymbol{U}^{(1)} - \boldsymbol{U}^*}{\Delta t} = -\frac{1}{\rho_0}\nabla q^{(1)}, \tag{29}$$

where $\nabla = \left(\frac{\partial}{\partial x}, \frac{\partial}{\partial y}, \frac{\partial}{\partial z}\right)$, and $\boldsymbol{U}^{(1)} = (u^{(1)}, v^{(1)}, w^{(1)})^{\mathrm{T}}$ is the intermediate velocity after calculation in the first stage. It corrects $\boldsymbol{U}^* = (u^*, v^*, w^*)^{\mathrm{T}}$ by considering the nonhydrostatic gradient term in momentum equations Eqs (22), (23), and (27). The nonhydrostatic $q^{(1)}$ is given by solving the Poisson equation of nonhydrostatic pressure, which can be derived by combining Eqs (25) and (29).

In the second stage, the projection is conducted again, and we can get the final value at the $n+1$ time level of the Runge–Kutta algorithm.

$$\frac{\boldsymbol{U}^{**} - \boldsymbol{U}^{(1)}}{\Delta t} = \boldsymbol{F}^{(1)}, \tag{30}$$

$$\frac{\boldsymbol{U}^{(2)}-\boldsymbol{U}^{**}}{\Delta t}=-\frac{1}{\rho_0}\nabla q^{(2)}, \tag{31}$$

$$\boldsymbol{U}^{n+1}=\frac{1}{2}\left(\boldsymbol{U}^{n}+\boldsymbol{U}^{(2)}\right), \tag{32}$$

where $\boldsymbol{U}^{**}$ and $\boldsymbol{U}^{(2)}$ play the same role as those in Eqs (28) and (29). Similar to solving Eq. (28) in step 1, the simplification will reduce the computation one more time when solving Eq. (30).

2.3 *Evaluation methods for the nonhydrostatic effect*

To evaluate the performance of the simplified nonhydrostatic model when simulating nonhydrostatic processes, we can consider it from two aspects. On the one hand, the difference between the simplified nonhydrostatic and hydrostatic models should be significant. More considerable differences indicate a more substantial nonhydrostatic effect. On the other hand, the results of the simplified nonhydrostatic model should be consistent with those of the fully nonhydrostatic model.

As such, we choose two parameters to evaluate the simplified nonhydrostatic model in this paper. One is the normalized root-mean-square error (NRMSE), defined as

$$\mathrm{NRMSE}=\sqrt{\frac{\sum_{i=1}^{N}\left(X_i^{R1}-X_i^{R2}\right)^2}{\sum_{i=1}^{N}\left(X_i^{R2}\right)^2}}, \tag{33}$$

where X^{R1} and X^{R2} are the results from two different models. R_1 and R_2 represent the nonhydrostatic and hydrostatic models, respectively. N is the grid number. A larger value of NRMSE indicates a stronger nonhydrostatic effect. If NRMSE >0.1 we think that the nonhydrostatic effect is obvious.

The other parameter is the Pearson correlation coefficient. For one-dimensional parameters, it is calculated by

$$r=\frac{\sum_{i=1}^{N}\left(A_i-\bar{A}\right)\left(B_i-\bar{B}\right)}{\sqrt{\sum_{i=1}^{N}\left(A_i-\bar{A}\right)^2}\sqrt{\sum_{i=1}^{N}\left(B_i-\bar{B}\right)^2}}, \tag{34}$$

for two-dimensional parameters, it is calculated by

$$r=\frac{\sum_i\sum_j\left(A_{ij}-\bar{A}\right)\left(B_{ij}-\bar{B}\right)}{\sqrt{\left(\sum_i\sum_j\left(A_{ij}-\bar{A}\right)^2\right)\left(\sum_i\sum_j\left(B_{ij}-\bar{B}\right)^2\right)}}, \tag{35}$$

where A and B are the results from simplified nonhydrostatic and fully nonhydrostatic models, respectively. i and j are grid number indices for the vector or matrix. A larger correlation coefficient value r reflects better consistency between the simplified nonhydrostatic model and the fully nonhydrostatic model. We take $r \geqslant 0.9$ as good and $r \geqslant 0.99$ as the very good performance of the simplification employed in this paper.

3 Numerical experiments

Two examples are made to test the nonhydrostatic simplification strategy in NHWAVE, including submesoscale surface sinusoidal waves and tidally induced internal lee wave in a smoothly stratified fluid.

3.1 *Sinusoidal wave over the idealized East China Sea (ECS) topography*

The simplification strategy is first used to investigate surface wave propagating on an idealized East China Sea topography (Fig. 1e), specified as Application 1. The computational domain is 500 km long in the zonal direction and 20 km long in the meridional direction, with a uniform horizontal resolution of 1 km. In the vertical direction, there are 34 σ layers. A submesoscale sinusoidal wave with an amplitude of η_0=0.2 m and a period of T_{input}=360 s enters the computational domain from the open west boundary. At the eastern boundary, free slip condition is used. The horizontal and vertical viscosities were set to be constants of 10^{-2} m^2/s and 10^{-3} m^2/s, respectively.

The horizontal and vertical space is normalized by the maximum still water depth d to discuss the process in dimensionless form. Time is normalized by the period of the input wave T_{input}. Velocities are normalized by d/T_{input}. Since water elevations in the ECS are generally much smaller than the still water depth, we discuss the water elevation η normalized by the initial amplitude of the incident wave η_0.

The water elevations from the hydrostatic, fully nonhydrostatic, and simplified nonhydrostatic models at nondimensional time instants of t=30.00, 30.25, 30.50, and 30.75 are shown in Figs 1a–d. Waves are presented as standing waves by interacting incident waves and waves reflected from the east boundary. The

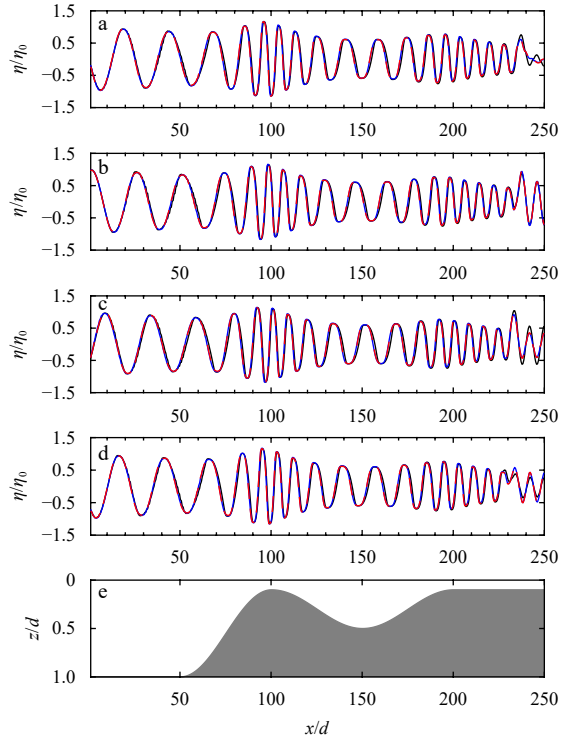

Fig. 1. Surface water elevation profiles of hydrostatic (black line), fully nonhydrostatic (blue line), and simplified nonhydrostatic experiment (red line) at time instant of t/T_{input}= 30.00, 30.25, 30.50, and 30.75, respectively (a–d); profile of the idealized ECS topography (e).

fully nonhydrostatic and simplified nonhydrostatic model results are very similar in the whole region, with a relative error of less than 1.5%, showing remarkable consistency. Locally, the relation between the wave amplitudes in two nonhydrostatic models and those in the hydrostatic model change with phase. In Figs 1a and c, two nonhydrostatic models have larger waves, while in Figs 1b and d, the hydrostatic models have larger waves. In the shelf region (x/d in the range of 200–250), the differences between the nonhydrostatic and hydrostatic model results are most apparent, which can be up to 100% in relative error (Fig. 1d).

Time series of surface water elevation in six sections with horizontal locations of x = 25, 50, 100, 150, 175, and 225 are given in Fig. 2 to further exhibit the variation of nonhydrostatic effect over time. In the nonhydrostatic model, the wave propagates more quickly. This effect accumulates as the wave propagates from the open boundary to the shelf region (Figs 2a–f) and finally influences the standing wave shape.

By using the NRMSE defined in Eq. (33) and the correlation coefficient r (defined in Eq. (34) for the one dimensional parameter) for surface water elevation, we can evaluate the performance of the simplified nonhydrostatic model. In Fig. 3a, the NRMSE for the fully nonhydrostatic and simplified nonhydrostatic models both grow with time in the same trend, indicating increasing nonhydrostatic effects. From Fig. 3b, the correlation coefficient r is very close to 1.0, it shows perfect consistency between the fully nonhydrostatic and simplified nonhydrostatic model results. Overall, the performance of the simplified nonhydrostatic model is excellent in this case.

3.2 *Tidally induced internal lee wave*

Internal lee waves generated by flow over topography are simulated to test the simplified model in a stratified fluid, specified as Application 2. Xing and Davies (2006a, b) first described this experiment to approximate the tidally induced internal lee wave process over a sill at the entrance to Loch Etive. Similar numerical studies have been conducted by Berntsen et al. (2006, 2008, 2009), Davies et al. (2009), Xing and Davies (2010) and Liu et al. (2016) to analyze the tidally induced mixing or nonhydrostatic effect. The above study show that internal lee waves are generated only during the flood time in the leeside of sill, controlled by the forcing flow in the upstream. Nonhydrostatic effects influence the distribution of internal waves and the associated mixing. In this study, we focus on the similarity of instantaneous velocity and density fields simulated by different version of models in the flood time. The topography and initial stratification are set similar to those in Berntsen et al. (2009), as shown in Fig. 4. To be consistent with previous studies, we discuss this application case in dimensional form. The computational domain is quasi-two-dimensional in the x-z direction. The resolution in the horizontal x-direction is 10 m, making a grid number of 2 150. There are 40 uniform σ layers in the vertical direction, making vertical resolutions of 0.375–2.5 m, varying with topography. As studied by Berntsen et al. (2009), tidally driven flow over sill and the wave field can be accurately resolved with such grid resolutions. The initial stratification of fluid is configured by a constant buoyancy frequency N=0.01 s^{-1}. In the west open boundary, the M_2 tide is imposed by giving tidal flow velocities with M_2 tidal frequency in the form of $U = U_0 \sin(\omega_{M_2} t)$, with ω_{M_2} = 0.000 140 526 rad/s (corresponding to a tidal period of T=24.12 h), where U_0 is the tidal flow amplitude. The external value of stratification keeps

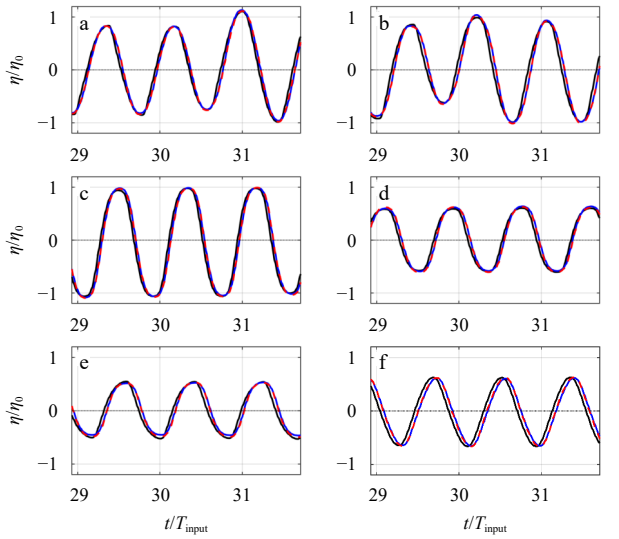

Fig. 2. Time series of surface water elevations from hydrostatic elevation (black line), fully nonhydrostatic (blue line), and simplified nonhydrostatic experiment (red line) at six stations. a–f correspond to x= 50, 75, 100, 125, 150 and 225, respectively.

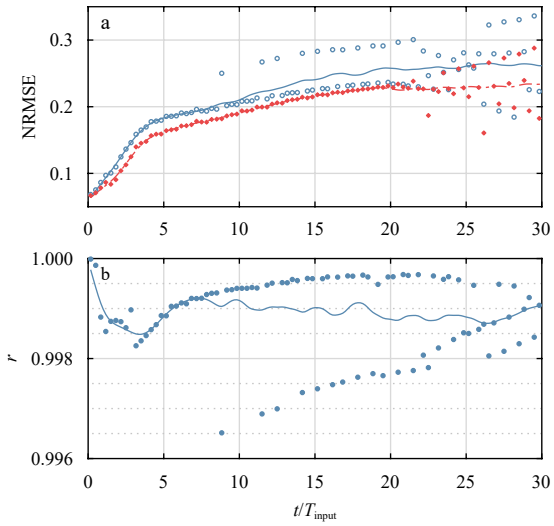

Fig. 3. Time series of NRMSE for water elevation, in which blue circles are for the fully nonhydrostatic model, with blue solid fitted curves; red asterisks are for the simplified nonhydrostatic model, with red dot-dash fitted curves (a); time series of the correlation coefficient r for water elevation between fully nonhydrostatic and simplified nonhydrostatic model results, in which curves are fitting results of numerical results (fitted circles) (b).

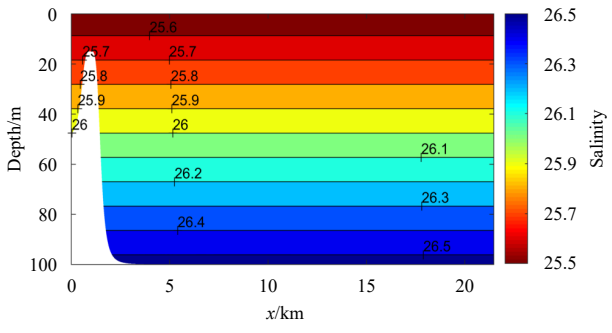

Fig. 4. The topography and initial salinity field distribution used in Application 2.

equal to the initial profile in the west open boundary. A sponge layer boundary condition is applied in the east boundary, such a condition is similar to the flow relaxation zone used by Xing and Davies (2010). Free slip conditions are adopted in other boundaries. The experiments are performed with constant value of viscosity as in Xing and Davies (2006) and Berntsen et al. (2009), that is: horizontal viscosity $A_H = 10^{-1}$ m^2/s, vertical viscosity $A_V = 10^{-3}$ m^2/s.

We examined the unsteady internal lee waves for three M_2 tidal cycles to reduce the transiens during the "spin up" time. A nearly uniform barotropic tidal cycle is established after an initial "spin up" period of one tidal cycle, which is consistent with Xing and Davies (2010). The generated internal waves are short both in period (of order minutes) and space (horizontal scale of order 100 m). Since irreversible mixing occurs in this process, fluid around the leeside of sill will become well-mixed in the third tidal cycle, and internal wave features become not apparent, so we took the results of the second tidal cycle to test the simplified non-hydrostatic model.

Initially, we set $U_0 = 0.3$ m/s, a typical velocity to approximate the maximum cross sill velocity in the Loch Etive (Inall et al., 2004). As tested (not shown), at $t = 5/4\ T$ (T is the M_2 tidal period), i.e., the flood time instant of second 1/4 M_2 tidal period, the major features are comparable as those in the first tidal cycle, except that mixing of fluid in the upper layer in the leeside of the sill is more explicit. Figure 5 shows the field snapshots of salinity, horizontal velocity in the x-direction, and vertical velocity at t=5/4 T from the fully nonhydrostatic model, the simplified nonhydrostatic model, and the hydrostatic model, respectively. From Fig. 5a, we can see that for all the three model results, two distinct regions on the leeside of the sill, the internal lee wave region (in the lower part) and the mixing region (in the upper part) for all three models. When tide propagates over the sill, internal waves are generated and propagate away from the leeside of the sill in the lower layer. The average depths and horizontal scale of internal waves are close to each other. Comparing with two nonhydrostatic models, the shape of the internal lee waves simulated by the hydrostatic model are more asymmetric. Internal waves simulated by the simplified nonhydrostatic model and fully nonhydrostatic models show good consistency.

In addition, vortices form periodically on the sill top next to the leeside. As they move away in the upper layer of the ocean, Kelvin-Helmholtz instability induces significant mixing in the surface and upper layers. Finally, the vortices will gradually dissipate and vanish as a result of the viscous effect. Vortices are generated more quickly in the hydrostatic model than in the nonhydrostatic model. In the lower panel of Fig. 5a, a vortex forms next to the top of the leeside in the hydrostatic model, this process will occur later in two nonhydrostatic models. Figures 5b and c show that the horizontal and vertical velocity components in the two nonhydrostatic models are closer to each other both for magnitude and phase, compared with those in the hydrostatic model.

Similar to Fig. 3 for Application 1, the NRMSE and the correlation coefficient r (defined in Eq. (35), for the 2D parameter) for salinity field in the former two tidal cycles are given in Fig. 6. The NRMSE in the fully nonhydrostatic and simplified nonhydrostatic models have similar trends of oscillating increase with time (Fig. 6a). The correlation coefficient of two nonhydrostatic models keeps larger than 0.9 (Fig. 6b) until after about t= 8/6 T. It decreases to about 0.8 late in the second tidal cycle, and even much lower after that. Since many reseachers also care about the short internal wave evolution in the first tidal cycle, the simplified nonhydrostatic model provides a very good approximation of fully

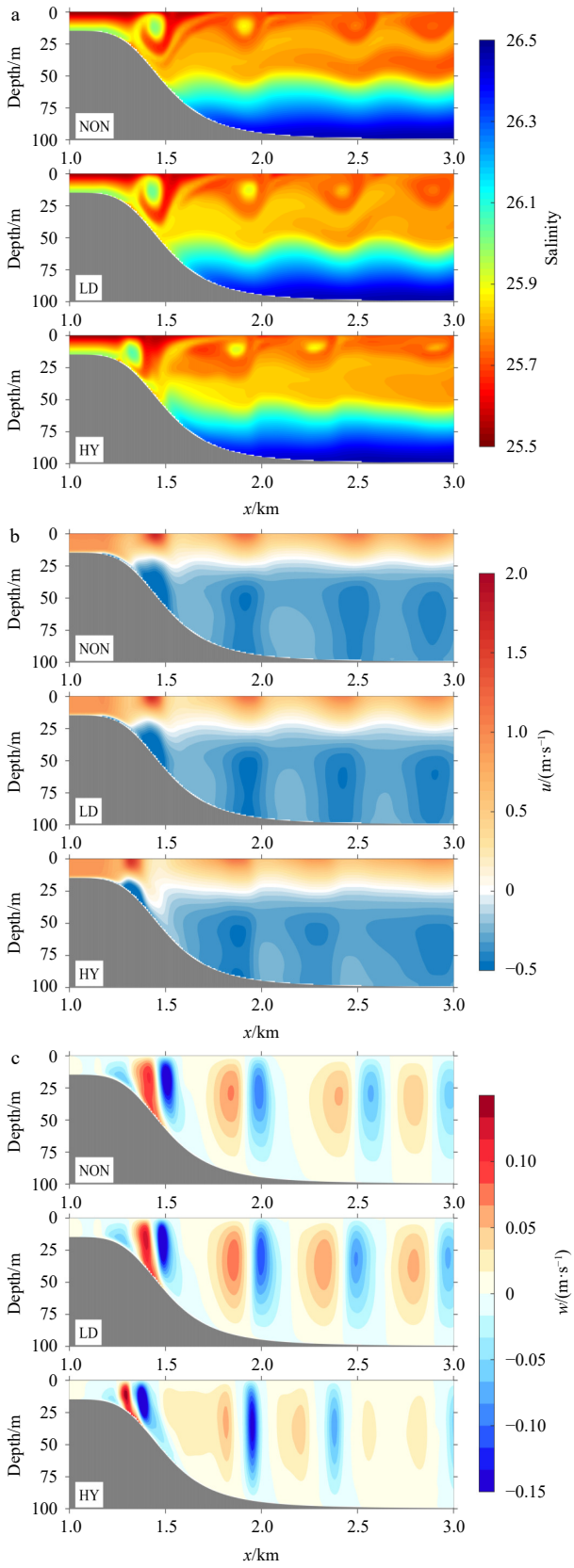

Fig. 5. Snapshots of field distribution for salinity (a), cross sill horizontal velocity (b), vertical velocity (c) at time instant of t=5/4 T, obtained from the nonhydrostatic model (NON), the simplified nonhydrostatic model (LD), and the hydrostatic model (HY), respectively.

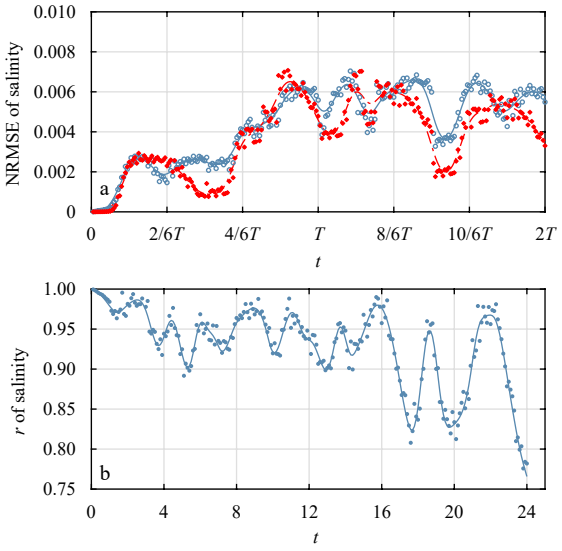

Fig. 6. Time series of NRMSE for salinity, in which blue circles are for the fully nonhydrostatic model, with blue solid fitted curves; red asterisks are for the simplified nonhydrostatic model, with red dot-dash fitted curves (a); time series of the correlation coefficient r for salinity between fully nonhydrostatic and simplified nonhydrostatic model results, in which curves are fitting results of numerical results (fitted circles) (b).

nonhydrostatic solution in this stage. During the second tidal cycle, though the correlation coefficient between the results of two nonhydrostatic models becomes not so good, especially during time late in the second tidal cycle, the simplified nonhydrostatic model can describes the distributation of salinity and velocity fields. The point-by-point correlation of two-dimensional salinity field may be a little bit hash, because it does not consider the influence of other factors, such as the phase difference of internal wave being generated.

4 Discussion

Numerical experiments in Section 3 have confirmed the prominent role of the local derivative in introducing nonhydrostatic effect, and the simplified nonhydrostatic model can obtain considerably good results for waves hundreds of meters long. To investigate the applicability of the simplification strategy, we will first extend the simplified nonhydrostatic model to a solitary wave simulation and see its performance in simulating a smaller scale wave. Then, we discuss the adaptability of this simplification to the case of different nonlinear strengths. An improvement in computational efficiency will also be introduced.

4.1 *Application of the simplification strategy to solitary wave over a slope*

As introduced before, solitary waves will form when the nonlinear steeping and nonhydrostatic dispersion come to a balance. We use the simplified nonhydrostatic model to simulate a smaller scale solitary wave propagating onto a beach, specified as Application 3. It is a phenomenon investigated many times numerically (Lynett et al., 2002; Ai and Jin, 2012) and experimentally (Synolakis, 1987). We would like to see if the simplification strategy works well in treating a smaller-scale phenomenon.

The entire domain is a two-dimensional space with a horizontal length of 11 m and a sloping beach in the eastern part. The still water depth varies from 0.21 m to 0.29 m with a beach slope

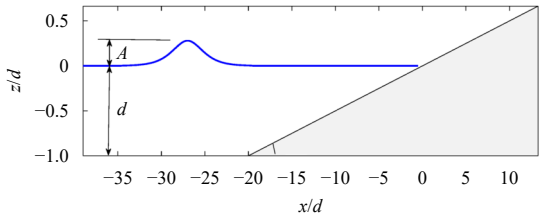

Fig. 7. A schematic diagram of solitary wave run-up model setup. A is the amplitude of the solitary incident wave, d is static water depth. The slope of the beach is 1:19.85.

of 1:19.85 (Fig. 7). The minimum water depth is 5 mm, which determines the wetting and drying of the computational cells. In the horizontal direction, 550 grids exist with a resolution of 0.02 m. Three layers are used in the vertical direction. As has been tested, when using more vertical layers, the results will not change much. Viscosity is ignored for simplicity. A solitary incident wave is imposed at the west open boundary.

As in Application 1, the horizontal and vertical scales are normalized by the maximum still water depth d. Time is normalized by the characteristic period of shallow-water waves $d/\sqrt{gd} = (d/g)^{1/2}$. Velocities can be normalized by $\sqrt{gd}$.

Case with dimensionless amplitude of $\frac{A}{d}$=0.3 is taken as an example to illustrate the process. Before the solitary wave reaches the edge of the beach (at nondimensional time instants of $t(g/d)^{1/2}$=8, 12, 16 in Fig. 8), it propagates in the water area with a flat bottom. For the hydrostatic model, the wavefront steepens from the very beginning because of the nonlinear effect. For the two nonhydrostatic models, however, the incident wave can nearly hold a solitary wave shape in both models, the wave amplitude of solitary waves only decrease by 1.6% and 7.3% in the fully nonhydrostatic model and simplified nonhydrostatic model, respectively, when the solitary wave reaches the edge of the beach. For the fully nonhydrostatic model, the decrease in amplitude may be caused by numerical dissipation in discretization. For the simplified nonhydrostatic model, numerical dissipation and omitting terms other than the local derivative take effect are responsible for that decrease.

After the incident wave comes to the edge of the beach at approximately $t(g/d)^{1/2}$=20, differences between the hydrostatic and

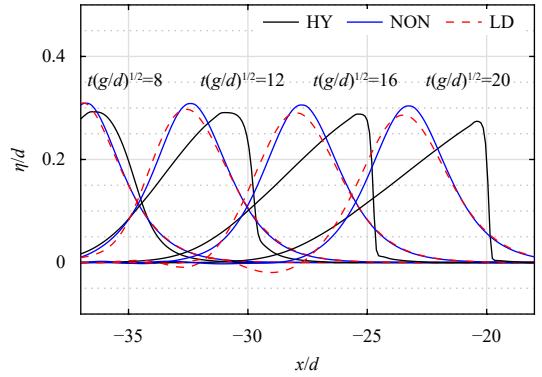

Fig. 8. Evolution of the normalized surface water elevation of a solitary wave propagating in the region with a flat bottom. Wave profiles from left to right denote time instants of $t(g/d)^{1/2}$=8, 12, 16, 20, respectively. The black, blue, and red lines represent the results from the hydrostatic, the fully nonhydrostatic, and the simplified nonhydrostatic simulations, respectively.

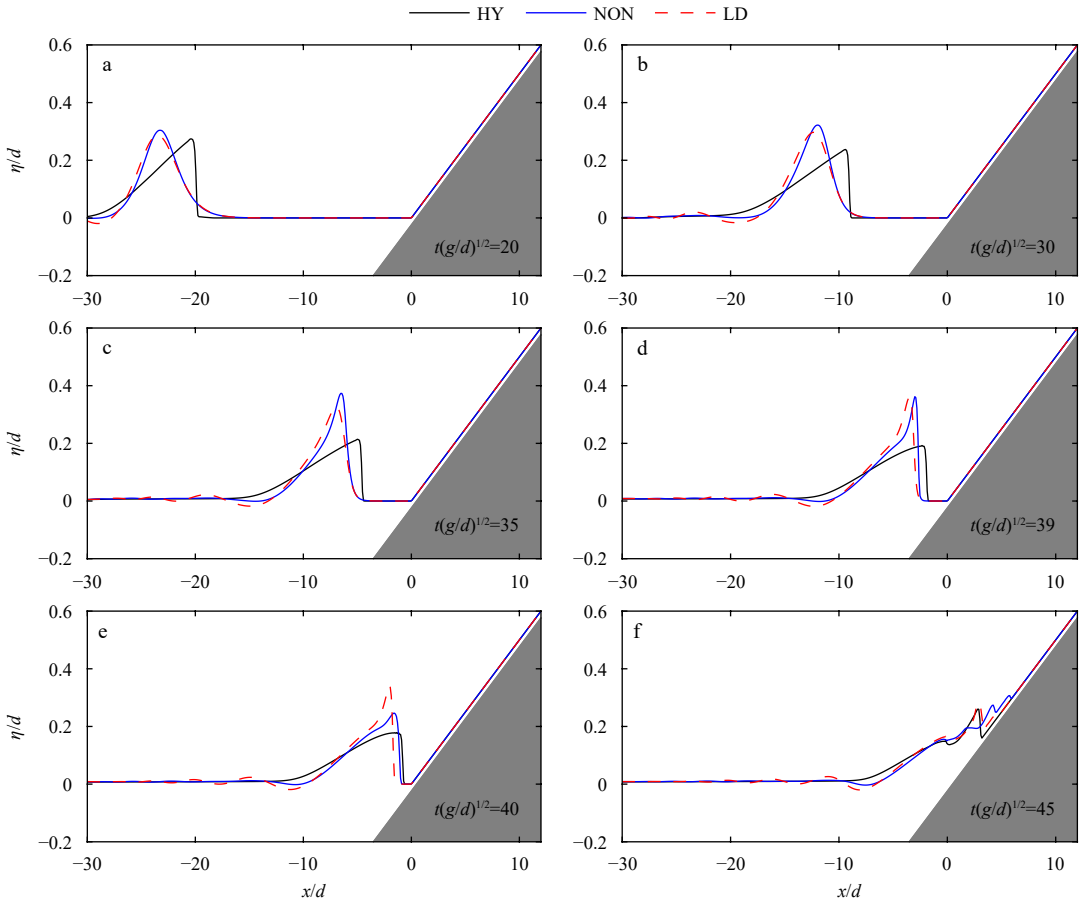

Fig. 9. Evolution of normalized surface water elevation η/d on the beach. a–f denote $t(g/d)^{1/2}$ ranging from 20 to 45. Lines legend represent results from the hydrostatic (HY), the fully nonhydrostatic (NON), and the simplified nonhydrostatic (LD) simulations, respectively.

two nonhydrostatic models become more apparent (Fig. 9). In the hydrostatic model simulation, the wavefront becomes nearly perpendicular to the static water surface, and the wave amplitude decreases monotonously. In both nonhydrostatic model simulations, the solitary wave gradually deforms, with the wavefront becoming steeper. At about $t(g/d)^{1/2}$=41, the wave reaches the coastline and breaks rapidly. The run-up height (perpendicular distance between the coastline and the maximum height of water run-up on the beach) is two times greater in the nonhydrostatic models than in the hydrostatic models.

Throughout the simulation, wave patterns in the fully nonhydrostatic model and the simplified nonhydrostatic model results are very similar, with nearly identical propagation speeds and steepness in the wavefront. The time-averaged relative difference in amplitude is no more than 5%, with the wave amplitude in the simplified nonhydrostatic model being smaller. In the simplified nonhydrostatic model result, a train of undular waves is generated in the backward wave direction but not in the fully nonhydrostatic model. It may be because the simplification employed in this paper influences the balance that supports solitary waves. These undular waves will take up the energy of the propagating solitary wave, which can explain why the wave amplitude in the simplified nonhydrostatic model is smaller.

As in Application 1, the NRMSE and correlation coefficient r for the water elevation is given in Fig. 10. The NRMSE first increases with time but at a decreasing acceleration. When the wavefronts reach the beach at approximately $t(g/d)^{1/2}$=38, the

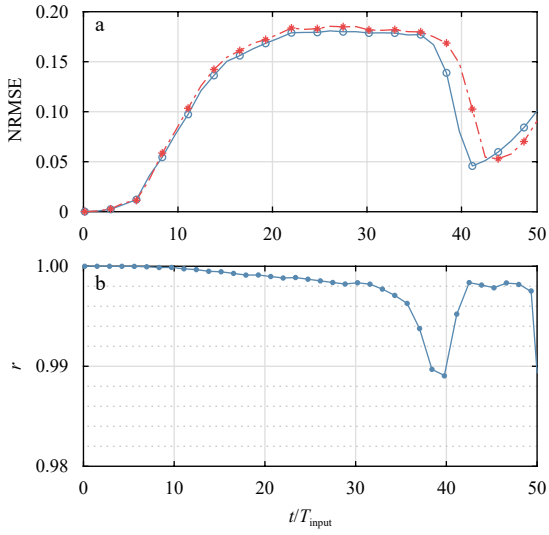

Fig. 10. Time series of NRMSE for water elevation, in which blue curve with circle markers is for the fully nonhydrostatic model; red curve with asterisk markers is for the simplified nonhydrostatic model (a); time series of the correlation coefficient r for water elevation between fully nonhydrostatic and simplified nonhydrostatic model results (b).

NRMSE of water elevation descends first and then rises, presenting a “V” shape. The correlation coefficients are almost all larger

than 0.99 (Fig. 10b). The results mean that the fully nonhydrostatic and simplified nonhydrostatic results are consistent.

4.2 *Applicability of the simplification influenced by nonlinearity*

Aricò and Re (2016) found in a Boussinesq model that numerical results will be closer to observations for higher nonlinear flooding processes if both the local derivative and convective term are retained rather than only the local derivative in the vertical momentum equation. Influences of nonlinearity are also found both in laboratory experiments and in numerical work. However, a broad conclusion in a three-dimensional model is still lacking. In this section, we adjust the nonlinearity in every application example to provide further discussion.

The nonlinear strength can be measured in different ways. For the surface wave experiments in Section 3.1 and Section 4.1, we use $\kappa = \frac{A}{d}$, in which A and d can be given by the surface wave amplitude and water depth, respectively. For the lee wave induced by stratified fluid flowing over topography in Section 3.2, we use $Fr = \frac{U}{Nh_0}$, in which N and U are the buoyancy frequency and the background velocity, respectively, and h_0 is the height of the topography. Both parameters indicate increasing nonlinearity when they become larger. We adjusted model parameters for Applications in Section 3 and Section 4.1 and discussed the performances of the simplified nonhydrostatic model. $\kappa = \frac{A}{d}$ is adjusted by changing A, and $Fr = \frac{U}{Nh_0}$ is adjusted by changing the incident velocity U at the west open boundary. The model setup and nonlinearity parameters for every application are listed in Table 5. Ranges of the parameters are set referring to previous studies of every specific application

For Application 1, the NRMSE and the correlation coefficient r for cases of different nonlinear strengths are shown in Fig. 11. Larger values $\frac{A}{d}$ correspond to larger NRMSEs (Fig. 11a). The correlation coefficient r departs with different nonlinear strengths

Table 5. A summary of model setup with different nonlinearity

Application 1: Surface sinusoidal wave			
Case	A/m	d/m	Nonlinearity parameter $\kappa = \frac{A}{d}$
1	2	2 000	0.001
2	10	2 000	0.005
3	14	2 000	0.007
4	18	2 000	0.009
5	20	2 000	0.010
Application 2: Tidally induced internal lee wave			
Case	U/(m·s^{-1})	h_0/m	N/s^{-1} Nonlinearity parameter $Fr = \frac{U}{Nh_0}$
1	0.1	85	0.01 0.12
2	0.3	85	0.01 0.35
3	0.9	85	0.01 1.06
Application 3: Solitary wave propagating onto a beach			
Case	A/m	d/m	Nonlinearity parameter $\kappa = \frac{A}{d}$
1	0.002 1	0.21	0.01
2	0.029 4	0.21	0.14
3	0.058 8	0.21	0.28
4	0.063 0	0.21	0.30
5	0.088 2	0.21	0.42
6	0.105 0	0.21	0.50

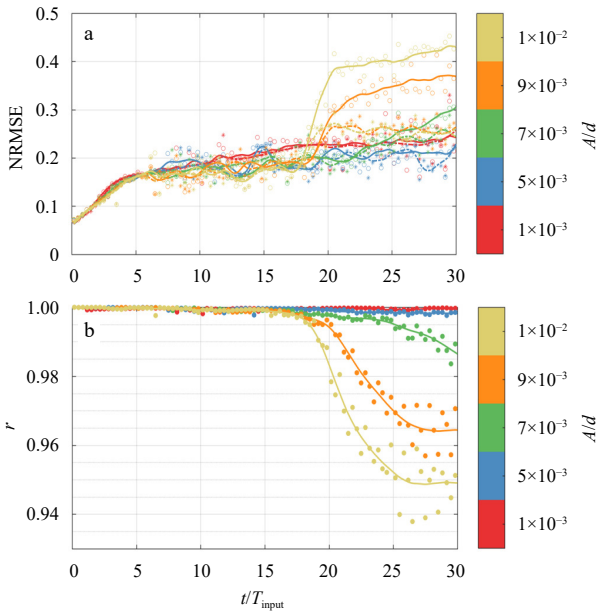

Fig. 11. Time series of NRMSE for surface water elevation with different nonlinear strengths, in which circles are for the fully nonhydrostatic model, with solid fitted curves; asterisks are for the simplified nonhydrostatic model, with dot-dash fitted curves. The color indicates nonlinear strength (a); time series of water elevation correlation coefficient r between fully nonhydrostatic and simplified nonhydrostatic model results with different nonlinear strength, with corresponding solid fitting lines (b).

(Fig. 11b). When the nonlinearity parameter $\frac{A}{d}$ is smaller than 5.0×10^{-3}, r is almost 1.0. As $\frac{A}{d}$ increases, r has a decreasing trend after t/T_{input} is approximately 15 (varying with cases). Nevertheless, it is always larger than 0.94 for cases with different nonlinear strengths, showing very good performance in the simplified nonhydrostatic model.

For Application 2, Fig. 12 shows salinity, horizontal velocity, and vertical velocity distributions with three different incident velocities (thus different nonlinearities, according to $Fr = \frac{U}{Nh_0}$) at t =5/4 T. When Fr increases, differences in field parameters between two nonhydrostatic model results become more apparent. When Fr increases to 1.06, both the internal lee wave field and the mixing regions in the upper layer are significantly different. The field parameters are more well mixed in the fully nonhydrostatic model results.

When $Fr = \frac{U}{Nh_0}$ increases (i.e., nonlinearity is stronger), the NRMSE and correlation coefficient r for salinity fluctuate with time more dramatically. The time averaged NRMSE and correlation coefficient r are given in Table 6. Overall, the NRMSE is larger when Fr becomes larger. When Fr increases, the correlation coefficients of results from the simplified nonhydrostatic and fully nonhydrostatic model decreases, showing worse performance of the simplified nonhydrostatic model. When Fr is 1.06, the correlation coefficient will drop quickly to lower than 0.9 within t=1/2 T. As Fig. 12 shows, the stratification and velocity fields from the simplified nonhydrostatic model differ from those in the fully nonhydrostatic model significantly. The above results indicate that the performance of the simplified non-hydrostatic model becomes poorer when nonlinearity increase.

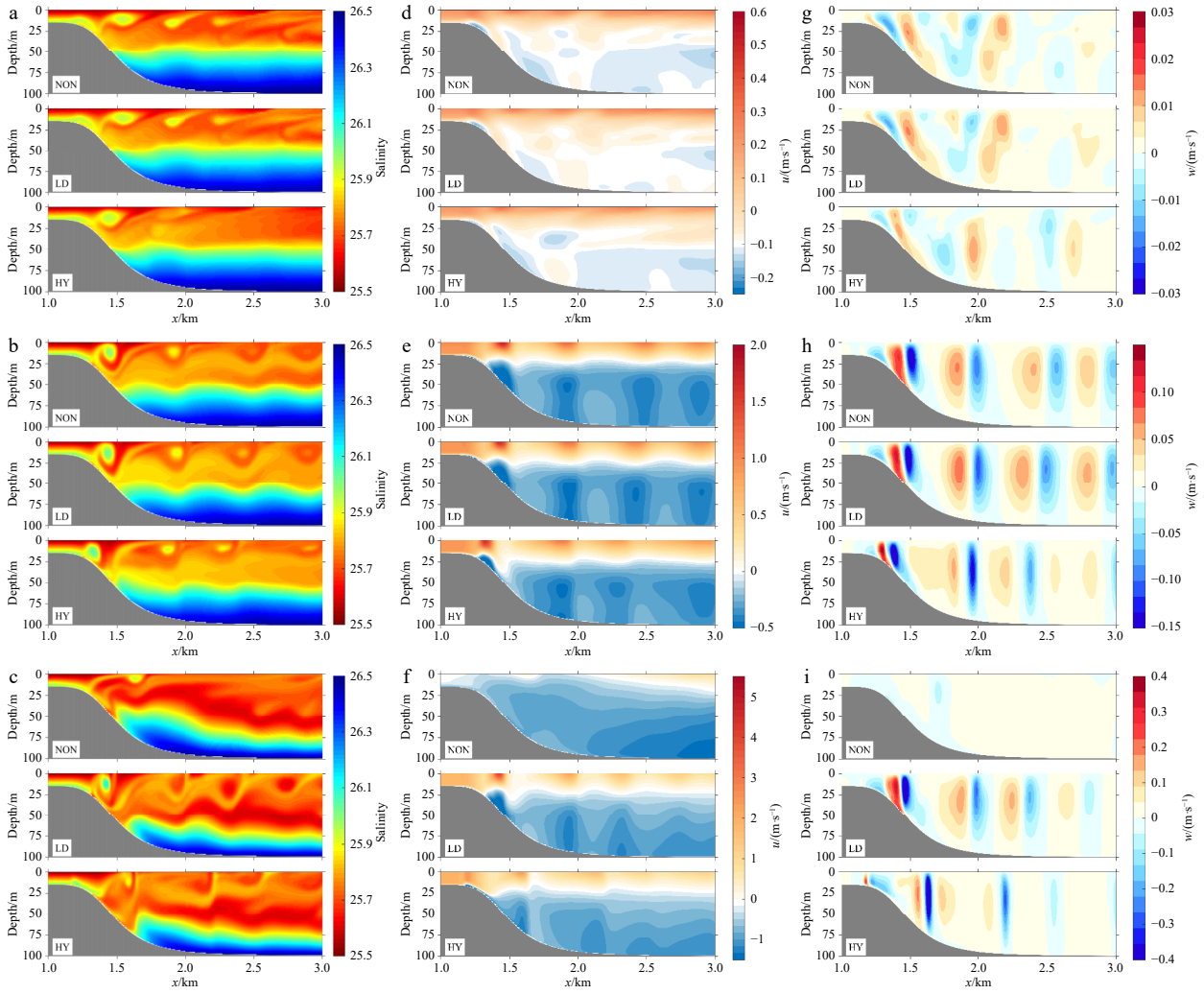

Fig. 12. The distribution of field parameters includes salinity, horizontal, and vertical velocity (every row) when Fr=0.12, 0.35, and 1.06 (every column). Three panels in every subplot a to i denote results from the nonhydrostatic model (NON), the simplified nonhydrostatic model (LD), and the hydrostatic model (HY), respectively (three panels).

Table 6. Time averaged NRMSE and correlation coefficient for salinity with different nonlinearities

$Fr=\frac{U}{Nh_0}$	NRMSE of NON[a] and HY[b]	NRMSE of LD[c] and HY	Correlation coefficient of NON and HY
0.12	3.4×10^{-3}	2.8×10^{-3}	0.92
0.35	5.5×10^{-3}	4.6×10^{-3}	0.90
1.06	1.2×10^{-2}	9.2×10^{-3}	0.48

Note: [a]NON denotes results from the fully nonhydrostatic model; [b]HY denotes results from the hydrostatic model; [c]LD denotes results from the simplified nonhydrostatic model.

For Application 3, the NRMSE and correlation coefficient for cases with different nonlinearities $\frac{A}{d}$ evolve similarly. The two fitting lines of the NRMSE are closer when $\frac{A}{d}$ are smaller (Fig. 13a). The correlation coefficients are all higher than 0.9 (Fig. 13b), which means that in this range of nonlinearity, the simplified nonhydrostatic model has good consistency with the fully nonhydrostatic model. Like in Application 1 and Application 2, the correlation coefficient r has a decreasing trend as the nonlinearity parameter becomes larger. For cases with different nonlinear strengths, r is almost larger than 0.9.

From the above three numerical examples, the nonlinearity parameters (in the form of $\kappa=\frac{A}{d}$ or $Fr=\frac{U}{Nh_0}$) are good indicators to predict the performance of the simplified nonhydrostatic model. Stronger nonlinearity tends to correspond to worse performance. A summary of the performance of the simplified nonhydrostatic model is given in Table 7.

Both Application 1 and Application 3 simulate surface waves and show similar behaviors. The results show that the correlation coefficients r in cases with different nonlinear strengths are almost all larger than 0.9, demonstrating the good performance of the simplified nonhydrostatic model. For the internal lee wave example in Application 2, the result is not as good as those in Applications 1 and 3. Take the nonlinearity parameter of approximately 0.35 as an example. The correlation coefficient r in Application 2 decreases to 0.95 at the time instant of the 1/2 tidal period, while in Application 3, it is very close to unity, even at a long time instant.

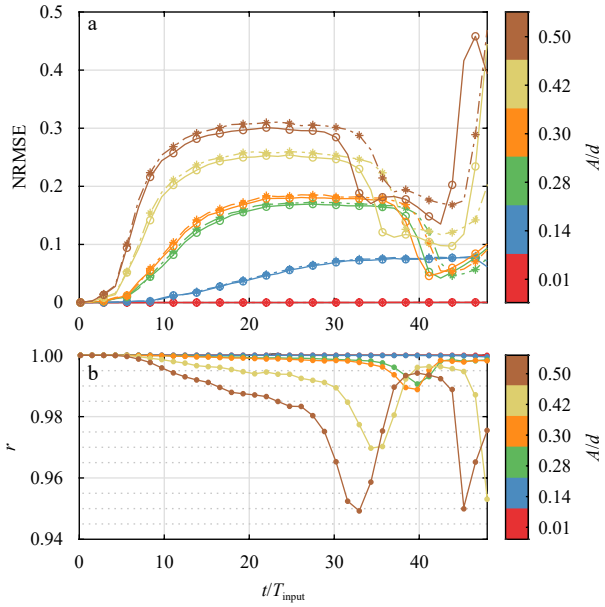

Fig. 13. Time series of NRMSE for surface water elevation with different nonlinear strengths, in which solid curves with circle markers are for the fully nonhydrostatic model, dot-dash curves with asterisk markers are for the simplified nonhydrostatic model. The color indicates nonlinear strength (a); time series of water elevation correlation coefficient r between fully nonhydrostatic and simplified nonhydrostatic model results with different nonlinear strength (b).

The results indicate that the performance of the simplified nonhydrostatic model may apply worse for simulating internal waves than surface waves. For this reason, from the scale analysis for surface waves and internal waves in Section 2.1, we know that the most important term that introduces the nonhydrostatic effect is the local derivative term. The second most important term is the nonlinearity term (including advection and convection). For a long surface wave, the local derivative is three orders of magnitude larger than the nonlinearity terms for a long internal wave. However, the local derivative term is only two orders larger than nonlinearity. This indicates that the local derivative term has a lower level of prominence in the internal wave simulation, especially when nonlinearity becomes stronger. This should be an important reason why the simplified nonhydrostatic model has better performance in surface wave simulation than in internal wave simulation.

4.3 *Calculation efficiency*

From Section 2.2, when employing the simplification strategy to construct a simplified nonhydrostatic model, several terms in the vertical momentum equation are omitted, this will reduce computation in the simulation. Table 8 compares the CPU time duration of the hydrostatic, the simplified nonhydrostatic model, and the fully nonhydrostatic models for Applications 1–3. In a set of experiments for one application, we only adjust the input wave amplitude or the incident flow, it makes little difference in the computation efficiency. Thus, we only take the first case in every application (Table 5) as representatives to compare the CPU time duration.

All the numerical experiments are conducted on the same computing cluster with Intel (R) Xeon (R) Platinum 8168 dual-core (2.70 GHz) processors. Application 1 and Application 3 are calculated in serial mode. For Application 2, one numerical case (nonhydrostatic versions) takes more than 100 h even in parallel mode with the available computational resources, we take 72 cores uniformly to compare the computational efficiency of models. From Table 8, the CPU time durations of both nonhydrostatic models are much longer than those of the hydrostatic model, which manifests the significance of reducing the computational burden in the nonhydrostatic model. By using the simplified nonhydrostatic model, the time durations for simulations in the fully nonhydrostatic model decrease by 16.4%, 17.9%, and 20.6% for Applications 1–3, respectively, showing reasonably good improvement in computational efficiency. Since the three-dimensional models often need a significant amount of calculation, this saving rate of computational time will be substantial.

The specially designed algorithm based on the simplified nonhydrostatic equation may remarkably reduce the computational time, such as reducing the number of unknowns in the equation to be solved or developing new schemes for the finite volume method, and this deserves more effort in the future.

5 Conclusions

The simplification strategy of only retaining the local vertical derivative term to reflect the nonhydrostatic effect is examined in the frame of the three-dimensional nonhydrostatic model NHWAVE. The simplification is first validated by the scale analysis of submesoscale surface waves and internal waves. Numerical examples, including submesoscale surface sinusoidal waves, tid-

Table 7. Performance of the simplified nonhydrostatic model

	Applications	Range of nonlinearity	Nonlinearity	Correlation coefficient, r	Summary
1	surface sinusoidal wave	0.001–0.010	$\kappa \leqslant 0.007$	$r \geqslant 0.99$	very good
			$0.007 < \kappa \leqslant 0.010$	$r > 0.9$	good
2	tidally induced internal lee wave	0.12–1.06	$Fr \leqslant 0.35$	$r_{salinity} \geqslant 0.9$	good
			$0.35 < Fr < 1.06$	$r_{salinity} < 0.9$	not good
3	solitary wave onto a beach	0.01–0.5	$\kappa \leqslant 0.14$	$r \geqslant 0.99$	very good
			$0.14 < \kappa < 0.5$	$0.90 < r < 0.99$	good

Table 8. Comparison of CPU time in different models

	Applications	Grid number $Nx \times Ny \times N\sigma$[a]	CPU time/s			Fully − Simplified / Fully
			Hydrostatic	Simplified nonhydrostatic	Fully nonhydrostatic	
1	surface sinusoidal wave	500×20×34	2.10×10^3	5.10×10^4	6.13×10^4	16.4%
2	tidally induced internal lee wave	2 150×40 (72 cores)	7.11×10^4	4.78×10^5	5.82×10^5	17.9%
3	solitary wave onto a beach	500×1×3	2.70×10	2.70×10^2	3.40×10^2	20.6%

Note: [a]Nx, Ny, $N\sigma$ represent grid numbers in horizontal x-direction, y-direction, vertical direction, respectively.

ally induced internal lee waves, and the solitary wave run-up process, are conducted to further validate the performance of the simplified nonhydrostatic model.

The results show that the simplified nonhydrostatic model can significantly improve hydrostatic simulation results, showing prominent nonhydrostatic properties for surface and internal submesoscale wave phenomena. At the same time, consistency between the simplified nonhydrostatic and fully nonhydrostatic model results is good. The simplification strategy can obtain good results even in a smaller scale process.

Nonlinearity influences the performance of the simplified nonhydrostatic model. When nonlinear strength becomes stronger, the performance of the simplified nonhydrostatic model will be worse. Overall, the simplified nonhydrostatic model can simulate the surface wave better than the internal wave. It is also proven that the computing time will decrease by 16.4%–20.6% when using the simplification in this paper.

References

Ai Congfang, Jin Sheng. 2012. A multi-layer non-hydrostatic model for wave breaking and run-up. Coastal Engineering, 62: 1–8, doi: 10.1016/j.coastaleng.2011.12.012

Ai Congfang, Ma Yuxiang, Yuan Changfu, et al. 2019. Development and assessment of semi-implicit nonhydrostatic models for surface water waves. Ocean Modelling, 144: 101489, doi: 10.1016/j.ocemod.2019.101489

Ai Congfang, Ma Yuxiang, Yuan Changfu, et al. 2021a. A three-dimensional non-hydrostatic model for tsunami waves generated by submarine landslides. Applied Mathematical Modelling, 96: 1–19, doi: 10.1016/j.apm.2021.02.014

Ai Congfang, Ma Yuxiang, Yuan Changfu, et al. 2021b. Non-hydrostatic model for internal wave generations and propagations using immersed boundary method. Ocean Engineering, 225: 108801, doi: 10.1016/j.oceaneng.2021.108801

Aricò C, Re C L. 2016. A non-hydrostatic pressure distribution solver for the nonlinear shallow water equations over irregular topography. Advances in Water Resources, 98: 47–69

Berntsen J. 2004. USERS GUIDE for a modesplit σ-coordinate numerical ocean model. Bergen: University of Bergen

Berntsen J, Xing Jiuxing, Alendal G. 2006. Assessment of non-hydrostatic ocean models using laboratory scale problems. Continental Shelf Research, 26(12/13): 1433–1447

Berntsen J, Xing Jiuxing, Davies A M. 2008. Numerical studies of internal waves at a sill: sensitivity to horizontal grid size and subgrid scale closure. Continental Shelf Research, 28(10/11): 1376–1393

Berntsen J, Xing Jiuxing, Davies A M. 2009. Numerical studies of flow over a sill: sensitivity of the non-hydrostatic effects to the grid size. Ocean Dynamics, 59(6): 1043–1059, doi: 10.1007/s10236-009-0227-0

Botelho D, Imberger J, Dallimore C, et al. 2009. A hydrostatic/non-hydrostatic grid-switching strategy for computing high-frequency, high wave number motions embedded in geophysical flows. Environmental Modelling & Software, 24(4): 473–488

Casulli V. 1999. A semi-implicit finite difference method for non-hydrostatic, free-surface flows. International Journal for Numerical Methods in Fluids, 30(4): 425–440, doi: 10.1002/(SICI)1097-0363(19990630)30:4<425::AID-FLD847>3.0.CO;2-D

Casulli V, Zanolli P. 2002. Semi-implicit numerical modeling of non-hydrostatic free-surface flows for environmental problems. Mathematical and Computer Modelling, 36(9–10): 1131–1149

Choi B J, Hwang C, Lee S H. 2014. Meteotsunami-tide interactions and high-frequency sea level oscillations in the eastern Yellow Sea. Journal of Geophysical Research: Oceans, 119(10): 6725–6742, doi: 10.1002/2013JC009788

Daily C, Imberger J. 2003. Modelling solitons under the hydrostatic and Boussinesq approximations. International Journal for Numerical Methods in Fluids, 43(2): 231–252

Davies A M, Xing Jiuxing, Berntsen J. 2009. Non-hydrostatic and nonlinear contributions to the internal wave energy flux in sill regions. Ocean Dynamics, 59(6): 881–897, doi: 10.1007/s10236-009-0217-2

Derakhti M, Kirby J T, Shi Fengyan, et al. 2015. NHWAVE: model revisions and tests of wave breaking in shallow and deep water. Newark: University of Delaware

Fringer O B, Gerritsen M, Street R L. 2006. An unstructured-grid, finite-volume, nonhydrostatic, parallel coastal ocean simulator. Ocean Modelling, 14(3–4): 139–173

He Dongbin, Ma Yuxiang, Dong Guohai, et al. 2020. Predicting deep water wave breaking with a non-hydrostatic shock-capturing model. Ocean Engineering, 216: 108041, doi: 10.1016/j.oceaneng.2020.108041

Inall M, Cottier F, Griffiths C, et al. 2004. Sill dynamics and energy transformation in a jet fjord. Ocean Dynamics, 54(3–4): 307–314

Kanarska Y, Maderich V. 2003. A non-hydrostatic numerical model for calculating free-surface stratified flows. Ocean Dynamics, 53(3): 176–185, doi: 10.1007/s10236-003-0039-6

Kanarska Y, Shchepetkin A, McWilliams J C. 2007. Algorithm for non-hydrostatic dynamics in the Regional Oceanic Modeling System. Ocean Modelling, 18(3–4): 143–174

Lai Zhigang, Chen Changsheng, Cowles G W, et al. 2010a. A nonhydrostatic version of FVCOM: 1. Validation experiments. Journal of Geophysical Research: Oceans, 115(C11): C11010, doi: 10.1029/2009JC005525

Lai Zhigang, Chen Changsheng, Cowles G W, et al. 2010b. A nonhydrostatic version of FVCOM: 2. Mechanistic study of tidally generated nonlinear internal waves in Massachusetts Bay. Journal of Geophysical Research: Oceans, 115(C12): C12049

Liu Zhe, Lin Lei, Xie Lian, et al. 2016. Partially implicit finite difference scheme for calculating dynamic pressure in a terrain-following coordinate non-hydrostatic ocean model. Ocean Modelling, 106: 44–57, doi: 10.1016/j.ocemod.2016.09.004

Lu Xinhua, Dong Bingjiang, Mao Bing, et al. 2015. A two-dimensional depth-integrated non-hydrostatic numerical model for nearshore wave propagation. Ocean Modelling, 96: 187–202, doi: 10.1016/j.ocemod.2015.11.001

Lynett P J, Wu T R, Liu P L F. 2002. Modeling wave runup with depth-integrated equations. Coastal Engineering, 46(2): 89–107, doi: 10.1016/S0378-3839(02)00043-1

Ma Gangfeng, Kirby J T, Shi Fengyan. 2013. Numerical simulation of tsunami waves generated by deformable submarine landslides. Ocean Modelling, 69: 146–165, doi: 10.1016/j.ocemod.2013.07.001

Ma Gangfeng, Shi Fengyan, Kirby J T. 2012. Shock-capturing non-hydrostatic model for fully dispersive surface wave processes. Ocean Modelling, 43–44: 22–35

Mahadevan A. 2006. Modeling vertical motion at ocean fronts: are nonhydrostatic effects relevant at submesoscales?. Ocean Modelling, 14(3–4): 222–240

Marshall J, Adcroft A, Hill C, et al. 1997a. A finite-volume, incompressible Navier Stokes model for studies of the ocean on parallel computers. Journal of Geophysical Research: Oceans, 102(C3): 5753–5766, doi: 10.1029/96JC02775

Marshall J, Hill C, Perelman L, et al. 1997b. Hydrostatic, quasi-hydrostatic, and nonhydrostatic ocean modeling. Journal of Geophysical Research: Oceans, 102(C3): 5733–5752, doi: 10.1029/96JC02776

Matsumura Y, Hasumi H. 2008. A non-hydrostatic ocean model with a scalable multigrid Poisson solver. Ocean Modelling, 24(1–2): 15–28

Shi Fengyan, Chickadel C C, Hsu TJ, et al. 2017. High-resolution non-hydrostatic modeling of frontal features in the mouth of the Columbia River. Estuaries and Coasts, 40(1): 296–309, doi: 10.1007/s12237-016-0132-y

Shi Jian, Shi Fengyan, Kirby J T, et al. 2015. Pressure decimation and interpolation (PDI) method for a baroclinic non-hydrostatic model. Ocean Modelling, 96: 265–279, doi: 10.1016/j.ocemod.2015.09.010

Shi Jian, Shi Fengyan, Zheng Jinhai et al. 2019. Interplay between grid

resolution and pressure decimation in non-hydrostatic modeling of internal waves. Ocean Engineering, 186: 106110, doi: 10.1016/j.oceaneng.2019.06.014

Stelling G, Zijlema M. 2003. An accurate and efficient finite-difference algorithm for non-hydrostatic free-surface flow with application to wave propagation. International Journal for Numerical Methods in Fluids, 43(1): 1–23, doi: 10.1002/fld.595

Synolakis C E. 1987. The runup of solitary waves. Journal of Fluid Mechanics, 185: 523–545, doi: 10.1017/S002211208700329X

Thomas L N, Tandon A, Mahadevan A. 2008. Submesoscale processes and dynamics. In: Hecht M W, Hasumi H, eds. Ocean Modeling in an Eddying Regime. Washington: American Geophysical Union, 17–38

Wei Zhangping, Jia Yafei. 2014. Non-hydrostatic finite element model for coastal wave processes. Coastal Engineering, 92: 31–47, doi: 10.1016/j.coastaleng.2014.07.001

Xing Jiuxing, Davies A M. 2006a. Processes influencing tidal mixing in the region of sills. Geophysical Research Letters, 33(4): L04603

Xing Jiuxing, Davies A M. 2006b. Influence of stratification and topography upon internal wave spectra in the region of sills. Geophysical Research Letters, 33(23): L23606, doi: 10.1029/2006GL028092

Xing Jiuxing, Davies A M. 2010. The effects of large and small-scale topography upon internal waves and implications for tidally induced mixing in sill regions. Ocean Dynamics, 60(1): 1–25, doi: 10.1007/s10236-009-0234-1

Yamazaki Y, Cheung K F, Kowalik Z. 2011. Depth-integrated, non-hydrostatic model with grid nesting for tsunami generation, propagation, and run-up. International Journal for Numerical Methods in Fluids, 67(12): 2081–2107, doi: 10.1002/fld.2485

Yamazaki Y, Kowalik Z, Cheung K F. 2009. Depth-integrated, non-hydrostatic model for wave breaking and run-up. International Journal for Numerical Methods in Fluids, 61(5): 473–497, doi: 10.1002/fld.1952

Zhang Z, Fringer O B, Ramp S R. 2011. Three-dimensional, nonhydrostatic numerical simulation of nonlinear internal wave generation and propagation in the South China Sea. Journal of Geophysical Research: Oceans, 116(C5): C05022

Zhou Zheyu, Yu Xiao, Hsu T J, et al. 2017. On nonhydrostatic coastal model simulations of shear instabilities in a stratified shear flow at high Reynolds number. Journal of Geophysical Research: Oceans, 122(4): 3081–3105, doi: 10.1002/2016JC012334

Zijlema M, Stelling G S. 2008. Efficient computation of surf zone waves using the nonlinear shallow water equations with non-hydrostatic pressure. Coastal Engineering, 55(10): 780–790, doi: 10.1016/j.coastaleng.2008.02.020

Zijlema M, Stelling G, Smit P. 2011. Simulating nearshore wave transformation with non-hydrostatic wave-flow modelling. In: Proceedings of the 12th International Workshop on Wave Hindcasting and Forecasting. Kona, HI: World Meteorological Organization